behavior is shown in Figure 8. At the reference pressure S_{hcg} = 0.02, as P_{pore} increases ($-\Delta P_{eff}$), gas dissolves in the oil and S_{hcg} decreases until ΔP_{eff} reaches -0.6 MPa, when all of the gas has dissolved in the oil. If P_{pore} decreases ($+\Delta P_{eff}$), gas comes out of the oil and S_{hcg} increases. This increase in S_{hcg} with $+\Delta P_{eff}$ accounts for the sharp gradients in ΔV_p seen in the upper portion of Figure 7a and 7b.

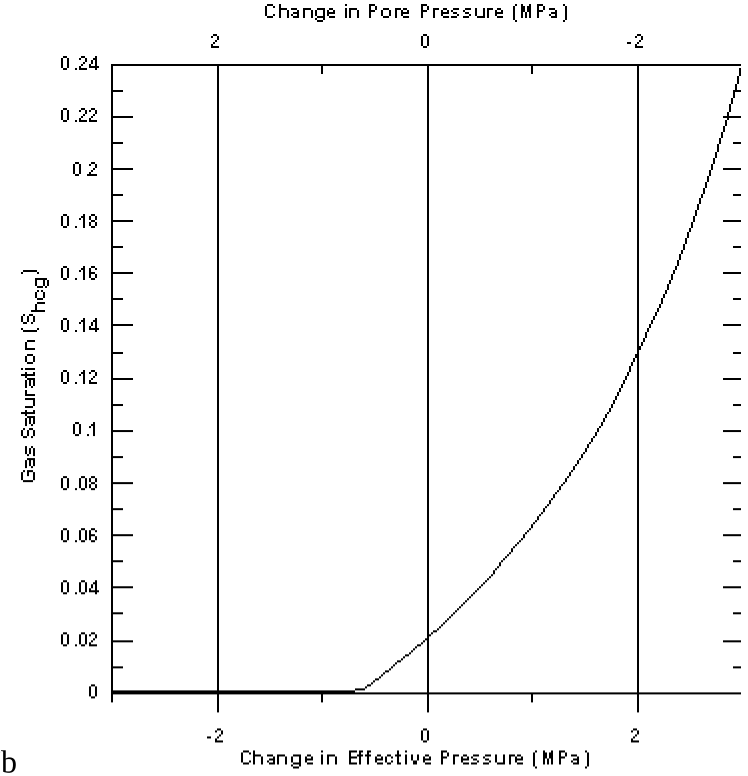

7b

Figure 8. *Change in S_{hcg} as a function of change in effective pressure for the model calculations shown in Figure 12. Reference S_w=0.5, S_{hcg}=0.02, f = 0.52?and P=4.7MPa.*

Although developed for hydrocarbon gas in oil, Equation (11) can be used to predict R_G^{max} for CO_2 if the appropriate gas gravity is used. Chung et al. (1988) present experimental results for CO_2 solubility in 22 API gravity oil at 66.7^o C over a range of pressures. The predicted values of R_G^{max} from Equation (11), using G_{grav}=1.51 for CO_2, are within 1% of the measured values over the range of P_{pore} found in the Lost Hills reservoir, between 800 and 1,500 psi. Based on this comparison, Equation (11) is appropriate for both hydrocarbon gas and CO_2. Data from Chung et al. (1988) also show that the amount of CO_2 that will dissolve in oil, at the relatively low temperatures and pressures in our experiment, is independent of the amount of hydrocarbon gas already dissolved in the oil. We will make use of this fact later in our interpretation of the observed velocity changes.

The dissolution of gas into oil as P_{pore} increases produces two opposite effects on the composite fluid bulk modulus (Equation (10)) and hence the bulk velocity of the rock. An increase in P_{pore} causes R_G^{max} to increase, allowing more gas to dissolve in the oil, lowering K_{oil} while at the same time reducing S_{hcg}. From Equation (10), we see that a decrease in K_{oil} and in S_{hcg} acts in opposition on K_{fluid}. In addition, an increase in P_{pore} (decrease in P_{eff}) reduces K_{dry} and G_{dry}, which reduces the bulk velocity of the rock. When S_{hcg} is small, decreasing S_{hcg} to zero increases the bulk velocity of the rock more than lowering K_{oil} (by dissolving gas) decreases it.

In contrast, decreasing P_{pore} increases K_{dry} which, by itself, would increase V_p. However, this effect is outweighed by the decrease in V_p caused by the increase in S_{hcg} as hydrocarbon gas comes out of solution from the oil. The net effect on V_p is seen in the upper halves of Figure 7a and 7b, where V_p decreases as P_{eff} increases (P_{pore} decreases).

PREDICTING TIME-LAPSE CHANGES IN RESERVOIR PARAMETERS

Before describing the process we have followed to estimate changes in fluid saturations, including *in situ* fluids and introduced CO_2, we acknowledge that the multitude of possible interactions between changes in pressure, hydrocarbon gas, and CO_2, as well as the effects on the oil from dissolved gas components, is too large to be uniquely determined from our geophysical measurements. We propose a procedure that makes use of a number of (what we consider to be) reasonable and most probable assumptions to estimate the change in CO_2 gas/oil ratio, ΔR_{CO2}, and CO_2 saturation, ΔS_{CO2}. The most critical assumption, supported by field reservoir engineers and operations staff (Perri, 2001), is that introduced CO_2 will dissolve in oil almost immediately after injection. Thus, we treat changes in the CO_2 gas/oil ratio as the primary mechanism for velocity reduction after changes in S_w and P have been accounted for.

EM data provide an independent estimate of ΔS_w. Electrical conductivity (σ) is a much simpler function of reservoir parameters than is velocity and can be described by Archie's law (Archie, 1942). Assuming ϕ is constant, $\Delta\sigma$ is only a function of ΔS_w and $\Delta\sigma_{brine}$. Because a water flood had been in effect for over 6 years at the start of CO_2 injection, we assume σ_{brine} has reached equilibrium between injected and native water and does not change. Therefore, conductivity changes are interpreted solely in terms of water saturation changes.

The process of converting the geophysical Δ images to Δ reservoir parameters begins with predicting ΔS_w between the wells from the $\Delta\sigma$?image, assuming that ϕ and σ_{brine} are constant. The predicted ΔS_w is used with the observed ΔV_s and the relation illustrated in Figure 7(c) to predict ΔP_{eff}. The process is illustrated schematically in Figure 9. At this point, the predicted ΔS_w and ΔP_{eff} sections have required only the assumption that $\Delta\sigma_{brine}$ does not change appreciably. Going beyond this point to use the observed ΔV_p with the predicted ΔS_w and ΔP to predict changes in CO_2 saturation, along with changes in absorbed gases, requires more assumptions and becomes riskier.

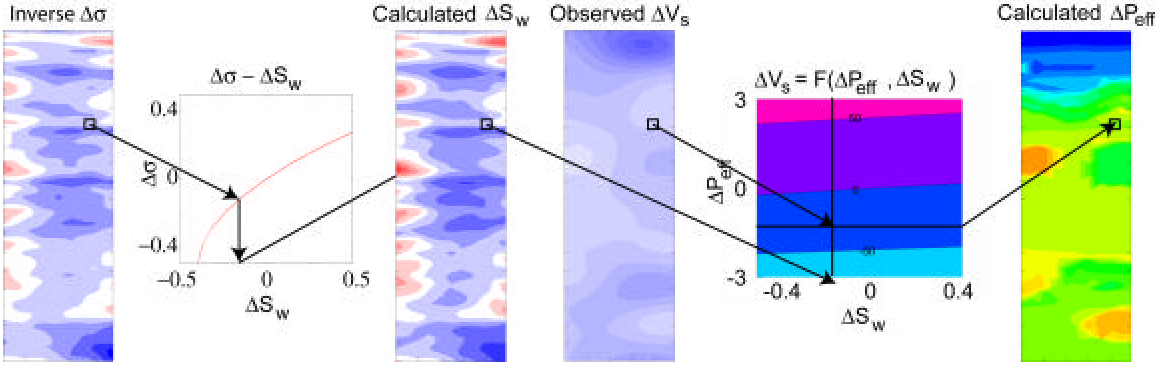

Figure 9: *Schematic diagram of process of estimating DS_w from inverse Ds and then using the estimated DS_w with the observed DV_s to estimate DP_{eff}*

The predicted ΔS_w and ΔP_{eff} are used to calculate the ΔV_p that results from ΔS_w and ΔP_{eff} alone, assuming $S_{hcg}=0$. Over the majority of the image plane, ΔS_w is negative, with the exception of small zones in the rind of water saturation which increase (as noted earlier).

Predicted ΔP_{eff} is negative over the entire interwell section, thus producing a $-\Delta V_p$. The residual change in velocity (ΔV_R) is defined by Equation (12):

$$\Delta V_R = \Delta V_p^{obs} - \Delta V_p^{calc} \ , \tag{12}$$

where ΔV_p^{obs} is the observed change in V_p and ΔV_p^{calc} is the calculated change in V_p. We expect the injected CO_2 to decrease V_p in excess of the effects of ΔS_w and ΔP_{eff} by dissolving CO_2 in oil and possibly producing $S_{co2} > 0$. Figure 10 schematically represents the process of calculating ΔV_R and using this with the rock properties model to estimate ΔR_{CO2}.

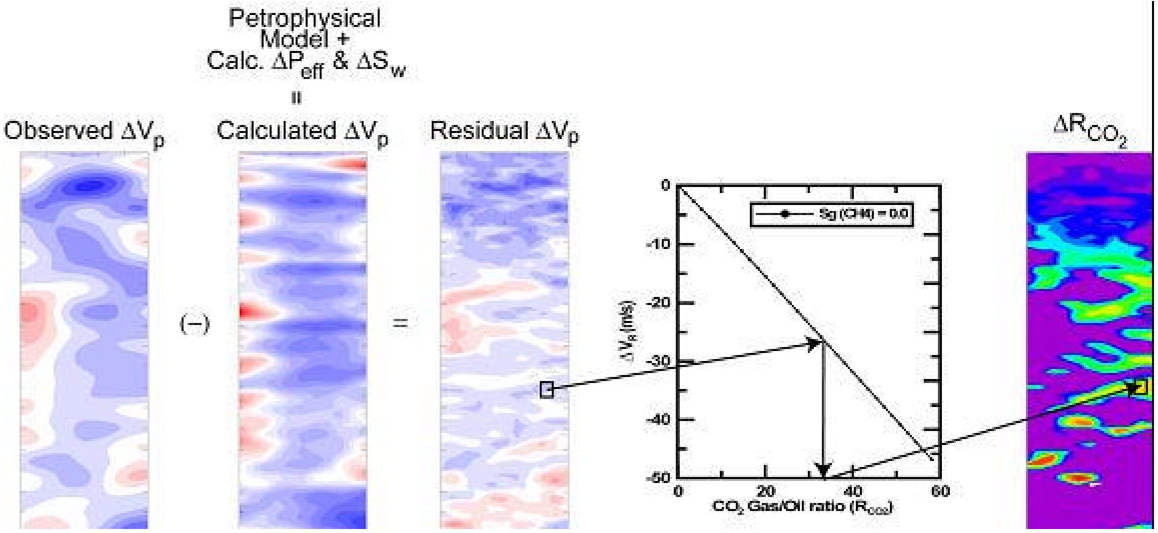

Figure 10: *Schematic representation of combination of* DV_R *and rock properties model to predict* DR_{CO2}.

On the other hand, a $+\Delta V_R$ can result if the assumption of no *in situ* hydrocarbon gas, S_{hcg}=0, is incorrect. This effect can be seen by comparing Figure 7a to 7b, where the presence of hydrocarbon gas reduces the change in V_p associated with a given ΔS_w and ΔP. As a consequence, a calculated ΔV_p, assuming $S_{hcg} = 0$ when $S_{hcg} > 0$, yields a calculated ΔV_p that is too large and hence a $+\Delta V_R$. However, if *in situ* hydrocarbon gas is present and has been accounted for in the calculation of ΔV_R, $+\Delta V_R$ can result if a P_{pore} increase causes hydrocarbon gas to dissolve in the oil , in which case S_{hcg} is reduced.

The OB-C1 log shows the presence of hydrocarbon gas over certain intervals within the reservoir. We noted a strong correlation between depth intervals with a non-zero S_{hcg} and $+\Delta V_R$. Therefore, a two-step process was used to calculate ΔV_R. The first pass used S_{hcg}= 0 as described. Next, sections of the image with $+\Delta V_R$ were recalculated assuming S_{hcg} = 0.02 (the average non-zero S_{hcg} in the reservoir interval). After the second pass calculation of ΔV_R, many of the areas that had $+\Delta V_R$ after the first pass calculations became negative, as ΔV_p^{calc} became less negative.

There are thus three regions of the ΔV_R section between the wells to interpret: (1) $S_{hcg} = 0$ and $\Delta V_R < 0$, (2) $S_{hcg} > 0$ and $\Delta V_R < 0$, and (3) $S_{hcg} > 0$ and $\Delta V_R > 0$. Regions of the crosswell section corresponding to $S_{hcg} = 0$ and $\Delta V_R < 0$ require an assumption about the partitioning of effects of free CO_2 and CO_2 dissolved in oil on $-\Delta V_R$. We chose to allow the maximum increase in R_{CO2}, as given by Equation (11), for the given ΔP_{pore} and ΔS_w. If the $+\Delta R_{CO2}$ does not completely account for the $-\Delta V_R$, then ΔS_{CO2} was calculated to account for the rest. For regions where $S_{hcg} > 0$ and $\Delta V_R < 0$, we assumed that the $+\Delta P_{pore}$ caused by injection would drive as much of the initial S_{hcg} into the oil as possible, followed by the same assumption about the partitioning of the $-\Delta V_R$ between $+\Delta R_{CO2}$ and ΔS_{CO2} as above. Regions where $S_{hcg} > 0$ and $\Delta V_R > 0$ were converted to $-\Delta S_{hcg}$.

Analysis shows that the oil is fully saturated with hydrocarbon gas at the ambient reservoir pressure. Therefore, we assume that the starting point for CO_2 absorption is oil with R_{hcg} at its maximum value for the given P_{pore} and T. As noted earlier, R_{CO2} and R_{hcg} are essentially independent, so that the oil can absorb the amount of hydrocarbon gas and CO_2 up to their respective $R_G^{\max}$, indicated by Equation (11). Because we lack an equation for calculating K_{oil} with two separate dissolved gases, we have assumed that Equation (13) is an adequate approximation of the bulk modulus of the oil:

$$K_{oil}^{co2+hcg} = K_{oil}^{dead} + \Delta K_{oil}^{co2} + \Delta K_{oil}^{hcg} \tag{13}$$

K_{oil}^{dead} is the oil bulk modulus without any gas, ΔK_{oil}^{co2} is the difference between K_{oil}^{dead} and the oil bulk modulus with CO_2 dissolved, and ΔK_{oil}^{hcg} is the difference between K_{oil}^{dead} and the oil bulk modulus with hydrocarbon gas dissolved.

Calculating $+\Delta R_{CO2}$ for regions where $\Delta V_R < 0$ is a simple linear interpolation between observed $-\Delta V_R$ and calculated $-\Delta V_R$ for a range of $+\Delta R_{CO2}$. If R_{CO2} reaches the maximum given by Equation (11), then the remaining observed $-\Delta V_R$ is used in a linear interpolation between calculated $-\Delta V_R$ over a range of $+\Delta S_{CO2}$ to calculate S_{CO2}.

The linear relation between ΔV_R and R_{CO2} is shown by the dotted line ($S_{hcg} = 0$) in Figure 11. In Figure 11, R_{CO2} increases from 0 to $R_{CO2}^{\max}$ from test number 1 to 34. From test number 34 to 41, S_{CO2} increases from 0 to 0.02, simulating the effect of progressively adding CO_2 that first dissolves in oil. After $R_{CO2}^{\max}$ is reached, CO_2 goes into the gas phase. Figure 9 also illustrates the effects of incorrectly assigning *in situ* hydrocarbon gas saturation. If $S_{hcg} > 0$ when $S_{hcg}=0.0$ is assumed, the estimated R_{CO2} will be low. On the other hand, if $S_{hcg}=0.0$ when $S_{hcg} > 0$ is assumed, the estimated R_{CO2} will be high. The error introduced by an incorrect S_{hcg} of 0.02 is approximately 15%.

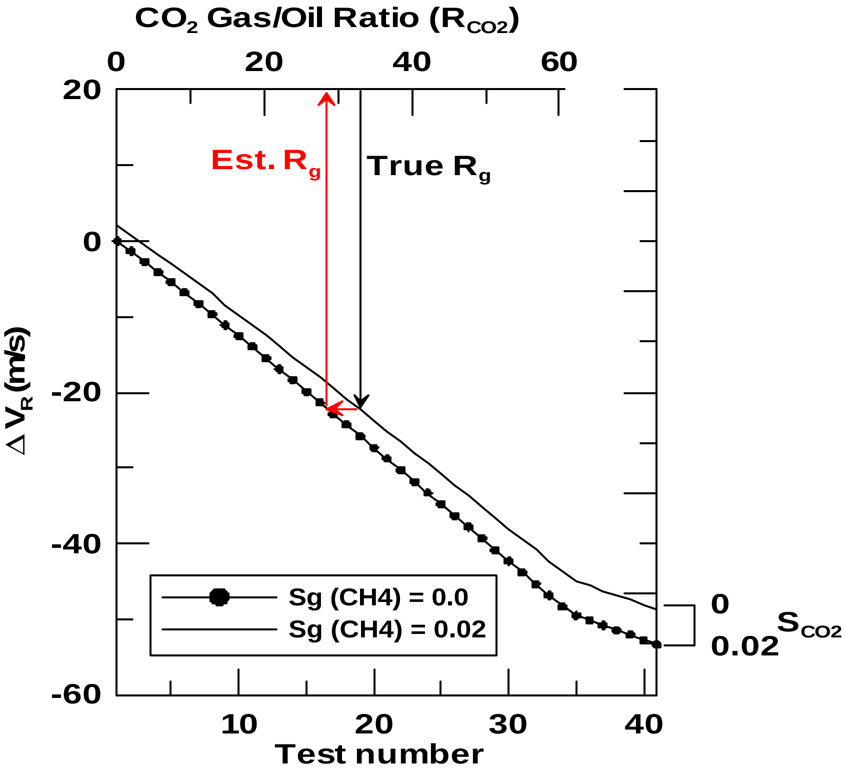

Figure 11. *DV_R as a function of R_{CO2} with and without hydrocarbon gas saturation, solid line is S_{hcg}=0.02, dotted line is S_{hcg}=0.0. The presence of S_{hcg} causes DV_R to be less negative than if S_{hcg}=0.0.*

Using this model, we have assessed the errors caused by incorrect values of the reference parameters S_w, ϕ, and P_{ref}. The error expressed as a percent of the true value is plotted in Figure 12 for the same R_{CO2} values used in Figure 11. A 15% perturbation of the true reference values were used, which we feel covers the expected variation in these

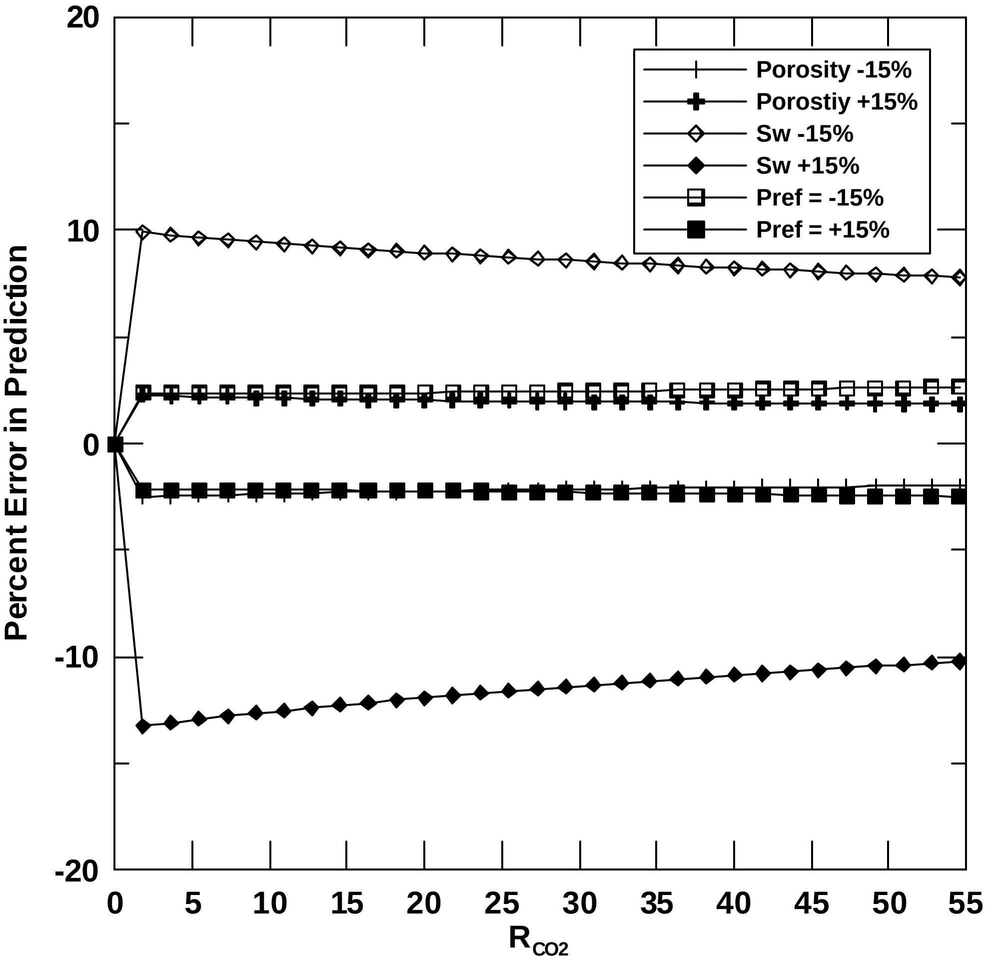

Figure 12. *Error in predicted R_{CO2} as a percentage of the true value. Reference values of porosity (f), water saturation (S_w) and effective pressure (P_{ref}) are in error by +-15%. The 15% range covers the expected variation in these parameters over the inter-well section.*

parameters over the interwell section. The error response as a function of R_{CO2} is approximately symmetric for positive and negative perturbations in the reference parameters used. The assumed S_w has the largest effect, followed by the assumed effective pressure, with the assumed porosity having the smallest effect. Overall, the estimated R_{CO2} is most sensitive to S_{hcg}, since an error of 0.02 in S_{hcg} causes a comparable error of 15% in S_w, but S_{hcg} may vary by more that 0.02.

Figure 13 shows the calculated absolute R_{CO2} (left side) and R_{CO2} expressed as a percent of $R_{CO2}^{\max}$ (right side) generated from the geophysical parameter changes shown in Figure 5, using the two-step process described above. Effective pressure from a history-matched flow simulation model and integrated density log at the beginning of CO_2 injection was used as the reference pressure. The predicted R_{CO2} never reached $R_{CO2}^{\max}$, so no S_{CO2} was needed to account for remaining $-\Delta V_R$. The predicted R_{CO2} shows a strong correlation with the location of perforation intervals (shown as black dots on the green CO_2 hydro-fracture line) that account for the majority of the injected CO_2. The percentage of injected CO_2 going into each perforation in the 11-8WR well (Figure 1) is plotted in the center of Figure 13 and shows that the upper four perforations account for 95% of all the CO_2. Almost 50% of the CO_2 goes into the uppermost perforation. The location of this perforation corresponds to the large $+R_{CO2}$

associated with the fault zone and region above, indicating loss of substantial CO_2 into the upper portions of the reservoir. The second, third, and fourth perforations from the top account for roughly another 45% of injected CO_2, with each perforation aligning with a laminar zone of $+R_{CO2}$. The only poor correlation between injected CO_2 and predicted $+R_{CO2}$ occurs at the perforation at a depth of 1,850 ft. At this depth, a laminar $+R_{CO2}$ zone aligns with a perforation, but the injectivity log indicates little injected CO_2. A possible explanation for this zone of increased CO_2 is the down-dip CO_2 injector 12-7W. This injector lies along the same hydraulic fracture azimuth as the 11-8WR (Figure 1) and shows considerable CO_2 injection into the geologic unit that intersects our image plane at 1,850 ft depth.

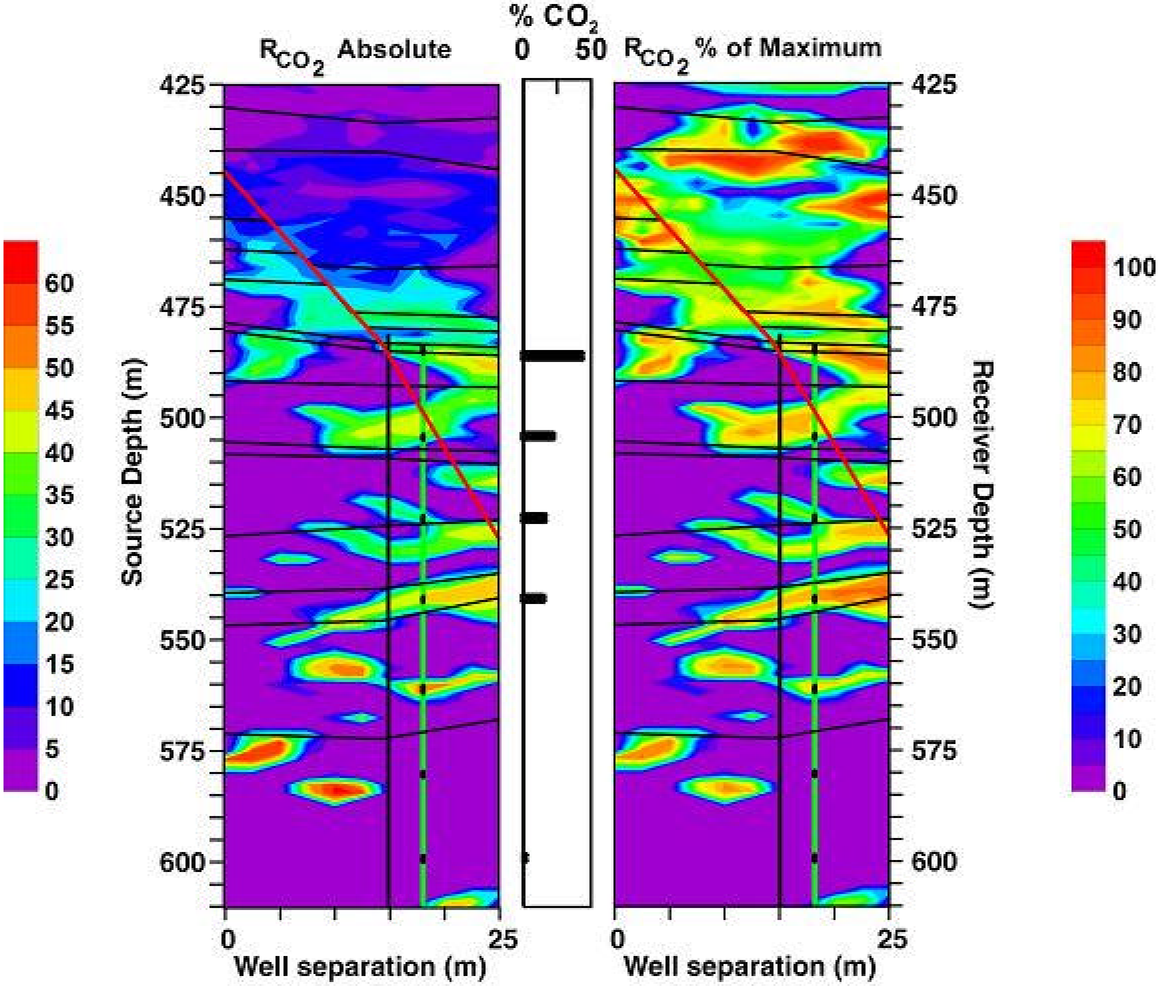

Figure 13. *Predicted CO_2/oil ratio (R_{CO2}). Left side shows absolute R_{CO2}, right side shows R_{CO2} as a percent of the maximum value for the given pressure and temperature. Major unit boundaries are shown as black sub-horizontal lines, estimated location of the previous water injection fracture is shown as a vertical black line, estimated location of the CO_2 injection fracture is shown as a vertical green line, perforation intervals for CO_2 injection are shown as black dots on top of the CO_2 injection fracture, and the mapped location of a fault zone is shown as a red diagonal line.*

The upper section of the fault (left side), where geologic-unit boundaries are offset, correlates with an increase in R_{CO2}, whereas the lower section (right side), where no displacements are mapped, does not. This is consistent with an increased permeability along portions of the fault that have significant movement compared to portions that do not. We interpret this image as indicating that CO_2 from the uppermost perforation is moving up dip along the fault zone and leaking into the high-permeability units above.

The image of R_{CO2} shown in Figure 13 has apparent higher vertical resolution of increased CO_2 zones compared to the geophysical anomalies shown in Figure 5. While there are zones of $-\Delta V_p$ associated with the same perforation intervals correlated with $+R_{CO2}$, there are additional areas of $-\Delta V_p$ above and below that do not correspond to $+R_{CO2}$. Because V_s is insensitive to the fluid substitutions (Figure 7c), we do not expect to see a correlation between ΔV_s and CO_2, either in the gas phase or dissolved in oil. Electrical conductivity changes will be related to changes in oil saturation through the change in S_w; these conductivity changes would also show a correlation to the displacement of water by oil, which may or may not be oil with dissolved CO_2 in it. Thus, although the $\Delta\sigma$ image (Figure 5) is correlated with the ΔV_p image, it also does not correlate with the injection intervals nearly as well as the derived R_{CO2} image of Figure 13. Overall, the R_{CO2} image has higher correlation with the injection intervals than the geophysical-change images and is also more horizontally stratified, as is the permeability structure of the formation.

CONCLUSIONS

We have used a rock-properties model, based on a close packing of spherical grains in conjunction with Gassmann's equation, to simulate the relationships between reservoir parameters of the Lost Hills diatomite and seismic compressional and shear velocities. A volumetric mixing law models bulk density. Parameters of the rock-properties model are derived by a simultaneous fitting of compressional velocity and density logs, using a simplex L1-norm minimization, given the observed porosity and fluid-saturation logs as well as measured pressure, temperature, and oil properties. Although the spherical grain model may not ideally represent the microscopic structure of the diatomite, the model accurately predicts the bulk seismic velocities and densities as a function of the fluid saturations, pressure, and porosity, as measured by log data and measurements made on core samples.

Calculations using the derived rock-properties model show that the rock bulk shear velocity primarily depends on pressure changes, with the effects of water saturation changes on shear velocity being of second order. Calculations also show that the presence of even a small amount of hydrocarbon gas strongly affects the relationships between V_p and the reservoir parameters. The influence of gas on compressional velocity makes it impossible to separate the effects of changes in hydrocarbon gas saturation, CO_2 gas saturation, and the effects on the oil caused by dissolved CO_2 on V_p without additional independent information. Crosswell EM data was used to provide estimates of changes in electrical conductivity that are directly related to changes in water saturation, thus providing an estimate of the change in water saturation that is independent from the seismic data.

To predict quantitatively the location and amount of CO_2 in the crosswell image plane, the change of P-wave velocity is decomposed into the part that can be predicted by the estimated changes in water saturation and pressure and the part predictable by a change in CO_2 content. The process relies on the assumption that the CO_2 will first dissolve in the oil and will only enter the gas phase after the oil has absorbed the maximum amount of CO_2 possible for the *in situ* pressure and temperature conditions. Using this procedure, we have demonstrated that by combining seismically derived changes in compressional and shear velocity with EM-derived changes in electrical conductivity, estimates of pressure change, water saturation change, and CO_2 gas/oil ratio can be made in a complex reservoir containing oil, water, hydrocarbon gas, and injected CO_2. The resulting predicted CO_2 /oil ratio, R_{CO2}, is better correlated with logged unit boundaries than are any of the images of changes in geophysical parameters. The size of the predicted CO_2-rich zones correlate with the amount of CO_2 that enters the formation through each perforation. The predicted ΔR_{CO2} images indicate that a significant portion of the injected CO_2 is filling the upper portions of the section above the intended injection interval. These conclusions are validated by CO_2 injectivity measurements made in the 11-8WR Well.

While we have tried to produce quantitative estimates of the CO_2 in place by estimating the CO_2/oil ratio, the values of this ratio depend on our assumptions about the partitioning of CO_2 between oil and gas phases. In addition, the assumed values of *in situ* hydrocarbon gas affect the estimates of the CO_2/oil ratio, so that the absolute values of our estimates may be in error. The main advantage of the approach described in this paper is the decoupling of the effects of pressure and water saturation changes from those caused by CO_2. This produces the improved spatial correlation between the estimated CO_2/oil ratio and the CO_2 injectivity logs when compared to the geophysical change images.

This analysis relies on many assumptions that were required because the project was not originally designed to use this methodology. In future applications, the number of assumptions could be substantially reduced by design. In particular, considerable benefit could be drawn from repeat logging of the wells with a full suite of logs. This would provide control points for the ΔP, ΔS_w, ΔS_g, ΔV_p, ΔV_s, and $\Delta\sigma$,?all of which would serve to greatly constrain the problem. Log measurements of the geophysical parameters would provide information for better starting models, with constraints on the velocity, density, and electrical conductivity at the well locations. Additionally, measurements of S_{CO2} and the amount of CO_2 dissolved in the oil would provide a basis for determining the partitioning of the residual velocity between the two, as well as eliminate the need to assume that all of the CO_2 dissolves in the oil before CO_2 gas is evoked as a mechanism of velocity change.

ACKNOWLEDGMENTS

Support for this work was provided by the Assistant Secretary for Fossil Energy, Office of Coal and Power Systems; Office of Oil, Gas and Shale Technologies, and through the National Energy Technology Laboratory under U.S. Department of Energy under Contract No. DE-AC03-76SF00098.

The authors are also grateful to Chevron Petroleum Co for providing data, and to Mike Morea and Pat Perri of Chevron for many helpful discussions. Mike Wilt of Electromagnetic Instruments and Barry Kirkendall of Lawrence Livermore National Laboratory provided crosswell EM data.

REFERENCES

Archie, G. E., 1942, The electrical resistivity log as an aid in determining some reservoir characteristics: Trans. Am. Inst. Mech. Eng., ***146****, 54-62.*

Batzle, M. and Wang, Z., 1992, Seismic properties of pore fluids: Geophysics, **57**, 1396-1408.

Bilodeau, B. J., 1995, Determining water saturation in diatomite using wireline logs, Lost Hills Field, California: SPE29653, in Proceedings of the Western Regional SPE Meeting, Bakersfield, CA, 369-382.

Brie, A., Pampuri, F., Marsala, A. F., and Meazza, O., 1995, Shear sonic interpretation in gas-bearing sands: SPE30595, in Proceeding of the SPE Annual Technical Conference, Dallas, Tx, 701-710.

Chung, F. T. H., Jones, R. A., and Burchfield, T. E., 1988, Recovery of viscous oil under high pressure by CO_2 displacement: A Laboratory Study: SPE 17588, in Proceedings of the SPE Annual Technical Conference, Tianjin,China, 401-410.

Dvorkin, J., and Nur, A., 1996, Elasticity of high-porosity sandstones: Theory for two North Sea datasets: Geophysics, **61**, 1363-1370.

Gassmann, F., 1951, Elasticity of porous media: Uber die Elastizitat poroser Medien: Vierteljahrsschrift der Naturforschenden Gesselschaft in Zurich, Heft 1.

Goudswaard, J. C. M., ten Kroode, A. P. E., Snieder, R. K. and Verdel, A. R., 1998, Detection of lateral velocity contrasts by crosswell traveltime tomography: Geophysics, **63**, 523-533.

Hashin, Z., and Shtrikman, S., 1963, A variational approach to the elastic behavior of multiphase materials: J. Mech. Phys. Solids, **11**, 127–140.

Harris, J. M., Nolen-Hoeksema, R. C., Langan, R. T., Van Schaack, M., Lazaratos, S. K., and Rector, J. W., 1995, High-resolution crosswell imaging in a west Texas carbonate reservoir: Part 1- Project summary and interpretation: Geophysics, **60**, 667-681.

Jackson, M. J., and Tweeton, D. R., 1996, 3DTOM: Three-Dimensional Geophysical Tomography: US Dept. of the Interior, Bureau of Mines, Report of Investigation 9617.

Landro, M., 2001, Discrimination between pressure and fluid saturation changes from time-lapse seismic data: Geophysics, **66**, 836-844.

Lazaratos, S. K., Harris, J. M., Rector J. W. and Van Schaack, M., 1995, High-resolution crosswell imaging of a West Texas carbonate reservoir: Part 4- Reflection imaging: Geophysics, **60**, 702-711.

Magee, J. W., and Howley, J. A., 1994, A predictive model for the thermophysical properties of carbon dioxide rich mixtures: Research Report RR-136, Gas Processors Association, Tulsa, OK.

Nemeth, T., Normark, E., and Qin, F., 1997, Dynamic smoothing in crosswell traveltime tomography: Geophysics, **62**, 168-176.

Newman, G. A., 1995, Crosswell electromagnetic inversion using integral and differential equations: Geophysics, **60**, 899-911.

Perri, P., 2001, Personal communication.

Rector W. J. ed., 1995, Special issue: Crosswell methods: Geophysics, **60**., No. 3.

Wang, Z., 2001, Personal communication.

Wang, Z., Cates, M. E. and Langan, R. T., 1998, Seismic monitoring of a CO_2 flood in a carbonate reservoir: A rock physics study: Geophysics, **63**, 1604-1617.

Wilt, M. J., Alumbaugh, D. L., Morrison, H. F., Becker, A., Lee, K. H., and Deszcz-Pan, M., 1995, Crosswell electromagnetic tomography: System design considerations and field results: Geophysics, **60**, 871-885.

Wood, A. W., 1955, *A Textbook of Sound*: The MacMillan Co., New York, 360pp.

TABLES

Table 1: *Definition of symbols.*

Parameter Name	Symbol	Parameter Name	Symbol
Dry frame bulk modulus	K_{dry}	CO_2 bulk modulus	K_{CO2}
Dry frame shear modulus	G_{dry}	Composite fluid bulk modulus	K_{fluid}
Effective dry frame bulk modulus	K_{eff}	Rock bulk density	ρ_{bulk}
Effective dry frame shear modulus	G_{eff}	Grain density	ρ_{grain}
Saturated rock bulk modulus	K_{sat}	Oil density	ρ_{oil}
Saturated rock shear modulus	G_{sat}	Brine density	ρ_{brine}
Grain bulk modulus	K_{grain}	CO_2 density	ρ_{CO2}
Grain shear modulus	G_{grain}	Gas correction	G_c
Grain Poisson ratio	n	Hydrocarbon gas density	ρ_{hcl}
Critical porosity	f_0	Rock bulk electrical conductivity	σ_{bulk}
Rock porosity	f	Brine electrical conductivity	σ_{brine}
Number of grain contacts	l	Archie porosity exponent	m
Water (brine) saturation	S_w	Archie saturation exponent	n
Oil saturation	S_o	Pore pressure	P_{pore}
Hydrocarbon gas saturation	S_{hcg}	Effective Pressure	P_{eff}
CO_2 saturation	S_{CO2}	Compressional velocity	V_p
Brine bulk modulus	K_{brine}	Shear velocity	V_s
Oil bulk modulus	K_{oil}	Gas/Oil ratio	R_g
Hydrocarbon gas bulk modulus	K_{hcg}	Gas gravity	G_{grav}

Table 2: *Rock-properties model parameters by model constituent. Model parameters fixed in the regression of well log data are shown in bold type. Asterisk (*) indicates that lithostatic pressure*

was calculated as a function of depth using the integrated density log, and pore pressure was taken as hydrostatic. Effective Pressure = Lithostatic – Hydrostatic Pressure.

Parameter Name	Symbol	Dry Frame Modulus	Gassmann's Fluid Substitution	Fluids	Electrical Conductivity	Regression Values
Grain Shear Modulus	G_{grain}	x				17.84 (Gpa)
Grain Poisson Ratio	n	x				0.107
Grain Density	ρ_{grain}	x	Dry Rock			2.358 (g/cc)
# of contacts/grain	l	x	K			3.68
Effective Pressure	P_{eff}	x				*
Critical Porosity	f_0	x				**0.55**
Pore Pressure	P_{pore}			x		*
Oil API gravity	API			x		**21.7**
Gas gravity	G_{grav}		Fluid K	x		0.585
Brine Salinity	S			x		**0.023 (PPM/10^6)**
Temperature	T			x		**42 (C)**
Fluid conductivity	σ_{brine}				x	0.23 (S/m)
Porosity exponent	m				x	-1.66
Saturation exponent	n				x	-1.85
Gas correction	G_c		x			0.0068943
*	Litostatic pressure from integrated density logs, P_{eff} = Litho - Hydro static					

2.4.4 Hyperspectral Geobotanical Remote Sensing for CO2 Storage Monitoring

CO_2 Capture Project - An Integrated, Collaborative Technology Development Project for Next Generation CO_2 Separation, Capture and Geologic Sequestration

Hyperspectral Geobotanical Remote Sensing for CO2 Storage Monitoring

Report Reference
2.4.4

Type of Report:	Semi-Annual Report
Reporting Period Start Date:	February 2003
Reporting Period End Date:	July 2003 2003
Principal Author(s):	Dr William L. Pickles
Date Report was issued:	August 2003
DOE Award Number:	DE-FC26-01NT41145
Submitting Organization:	Lawrence Livermore National Laboratory
Address:	University of California Lawrence Livermore National Laboratory 7000 East Ave L 644 Livermore CA 94550

2.4.4.1 Abstract

This project has the goal of providing a method of mapping for Co2 leaks by the effects on the plants the excess soil CO2 concentrations and for mapping hidden fault pathways for potential CO2 leaks, over the entire region above an underground formation being injected with CO2. The method we are developing uses airborne hyperspectral high-resolution imagery. We have collaborated with a commercial hyperspectral imagery provider in developing these techniques so that eventually the ongoing surveillance of a field can be contracted for commercially. This project is research collaboration between two University of California campuses, Lawrence Livermore National Laboratory (LLNL) and UC Santa Cruz (UCSC). The collaboration is large and involves the newly created Center for Remote Sensing at UC Santa Cruz. Two UCSC Professors, three graduate students, and a Senior Scientist at LLNL are working on this CO2 monitoring and surveillance project.

2.4.4.2 Table of Contents

2.4.4.3 Introduction

The hyperspectral geobotanical remote sensing techniques that we are developing use advanced commercial airborne imaging spectrometer systems now available in the USA and worldwide. The system that we normally contract for in our overhead imaging missions produces visible and near IR reflected light images with spatial resolution of 1 to 3 meters in 128 wavelength bands. The spatial resolution allows us to detect and discriminate individual species of plants as well as the complexities of the geological and man made objects in the images. We then can interpret the observed plant species distributions and their relative health along with a detailed understanding of the local geology, soil types, water and water conditions, and human activities. We are able to distinguish terrestrial and aquatic plant species, all types of geological formations and soil types, and many different types of human activities. We can then look for biological impacts of CO_2 leaks or seepages in large complicated areas such as estuaries, ports, rivers, deserts, forests, grasslands, farmlands, cities, industrial areas, etc. These techniques do not require before and after imagery because they use the spatial patterns of plant species and health variations present in the one image to distinguish slow leaks.

These techniques should allow us to distinguish the effects of small leaks from the damage caused to the biosphere by the other local human activities such as pipeline construction and natural factors such as storm run off. The plants in an area can accumulate small doses of leaked materials. The plant health and species modification spatial patterns do record time-integrated effects of small quantities of leaked CO_2. This can be important in finding leaks that would other wise are hard or impossible to detect by direct observation.

2.4.4.4 Executive Summary

During the last six months our hyperspectral imaging project for CO2 leakage monitoring has focused on using the extensive hyperspectral imagery set that we acquired of the Rangely CO enhanced oil recovery field in August 2002. We have accomplished extensive analysis of this imagery. We have created highly detailed maps of soil types, plant species, plant health, water conditions, and human activities. The results will be verified in a field trip to Rangely CO in August 2003. These maps establish an environmental and ecological baseline against which any future CO2 leakage effects on the plants soils and water conditions can be detected and verified. We have also seen signatures that may be subtle hidden faults. If confirmed these faults might provide pathways for upward CO2 migration if that occurred at any time during the future.

2.4.4.5 Experimental

The experimental method we are creating can be summarized as:
Determine the area above the formation to be monitored including some surrounding areas that are thought to be outside the influence of any CO2 that might percolate to the surface.
Work with the image acquisition contractor to develop a set of flight lines along which the images will be acquired.
If possible make a group trip to the area to start to become familiar with the special characteristics of the region at the time planned for the airborne overhead image acquisition.
Using GPS (Garmin 76 handheld with mapping) and digital cameras (Canon G2) visually record the soils, plants, minerals, waters, and manmade objects in the area.
Remain on location to be available to the pilots and image sensor operator while the imagery is being acquired. This is usually one day between 10:00 and 14:00. But it can be two days. We normally all meet at the aircraft before and after the day's flight to go over the plans and check results.
The sensor characteristics and a discussion of overhead hyperspectral imagery acquisition can best be seen at the web site of our imagery acquisition contractor. http://www.hyvista.com/

Figure 1. The hyperspectral sensor is shown in the aircraft used by our acquisition contractor for image acquisitions.

Figure 2 Ashley Hill is the acquisition contractor's sensor operator and flight commander. He is shown with the onboard computer system that controls the sensor systems and records the image, and the exact geolocation of each pixel in the image as it is acquired. The aircraft is the B300 Twin Otter.

Figure 3. Morning preparations of the B 300 Twin Otter aircraft, sensor, georectification system, and computer system for our hyperspectral image acquisitions. Note the absolutely clear skies which is ideal.

After the acquisition is completed our team reviews the imagery and georectification. Our acquisition contractor then sends it to their main facility Sydney Australia for final post processing.

The imagery set of all flight lines is returned to us on DVD's as three products; Raw, corrected to reflectance including atmospheric absorptions, and georectification control files. This usually takes less than a few weeks.

The imagery on the DVD's is analyzed using the ENVI commercial computer software on Windows and or UNIX platforms, by our researchers at UCSC, LLNL, and HyVista Corp, working as team. Please see the Research Systems Inc web site at http://www.rsinc.com/envi/index.asp for information about the ENVI program. Joe Board man and Fred Kruse wrote the ENVI program. Their website is at http://www.aigllc.com/ and is considered the standard for the hyperspectral image analysis community worldwide.

The imagery is analyzed to produce "maps" of plant species types, plant health within species types, soil types, soil conditions, water bodies, water contents such as algae or sediments, mineralogy of exposed formations, and manmade objects such as roads, buildings, playgrounds, etc. These "maps" are actually collections of individual georectified pixels.

The maps derived from the imagery analysis are the studied to look for species of plants where they would normally not be found, relative plant health patterns, altered mineral distributions, soil type distributions soil moisture distributions, water and water contents, and other categories.

We then return to the field with our analysis available in our laptop computers running ENVI to verify the results. Based on the verification results the analysis can be "fine-tuned" in the field to produce more accurate maps. Since the maps are georectified and the pixel size is 3 meters individual objects such as trees, outcropping minerals, jeep trails, well heads and pads can all be located using the maps and handheld a GPS. So the verified maps are extremely accurate.

2.4.4.6 Results and Discussion

We have done many analysis of the Rangely hyperspectral imagery using ENVI. We have combined these with the photos, topographic maps, and digital elevation models we have of the Rangely Oil field, town and surrounding areas.

Some of the highlights of this analysis work done to date are shown in the figures below.

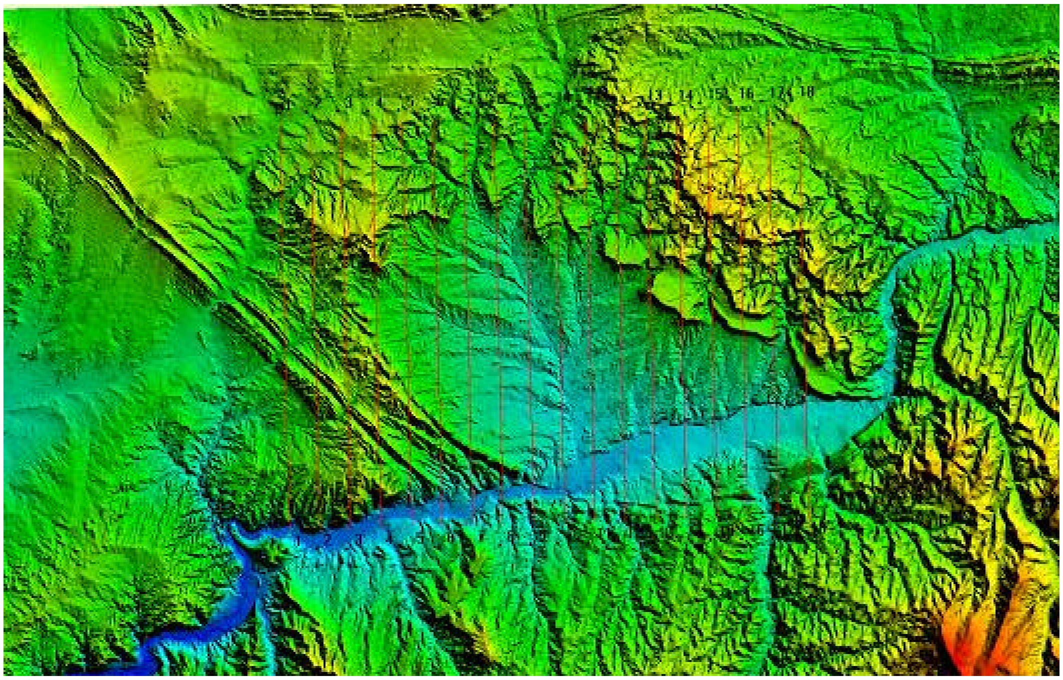

Figure 4 This is a digital elevation model of the Rangely Oil Field basin and surrounding formations. The White river basin is shown running from the center right to the lower left corner. The Rangel Oil field basin is in the center of the figure. The 18 flightlines that were flown to acquire the 18 strip images are shown in red. They are exactly due north and south by design. They are labeled 1 through 18. The town of Rangely CO is located in the White River Basin close to line 14. The folded formations whose motion created the oil field are easily seen running from southeast to northwest on either side of the basin and east west across the top. Mellen Hill and the Mellen Hill fault can be easily seen at the north west end of the oil field basin. (Done by Brigette Martini)

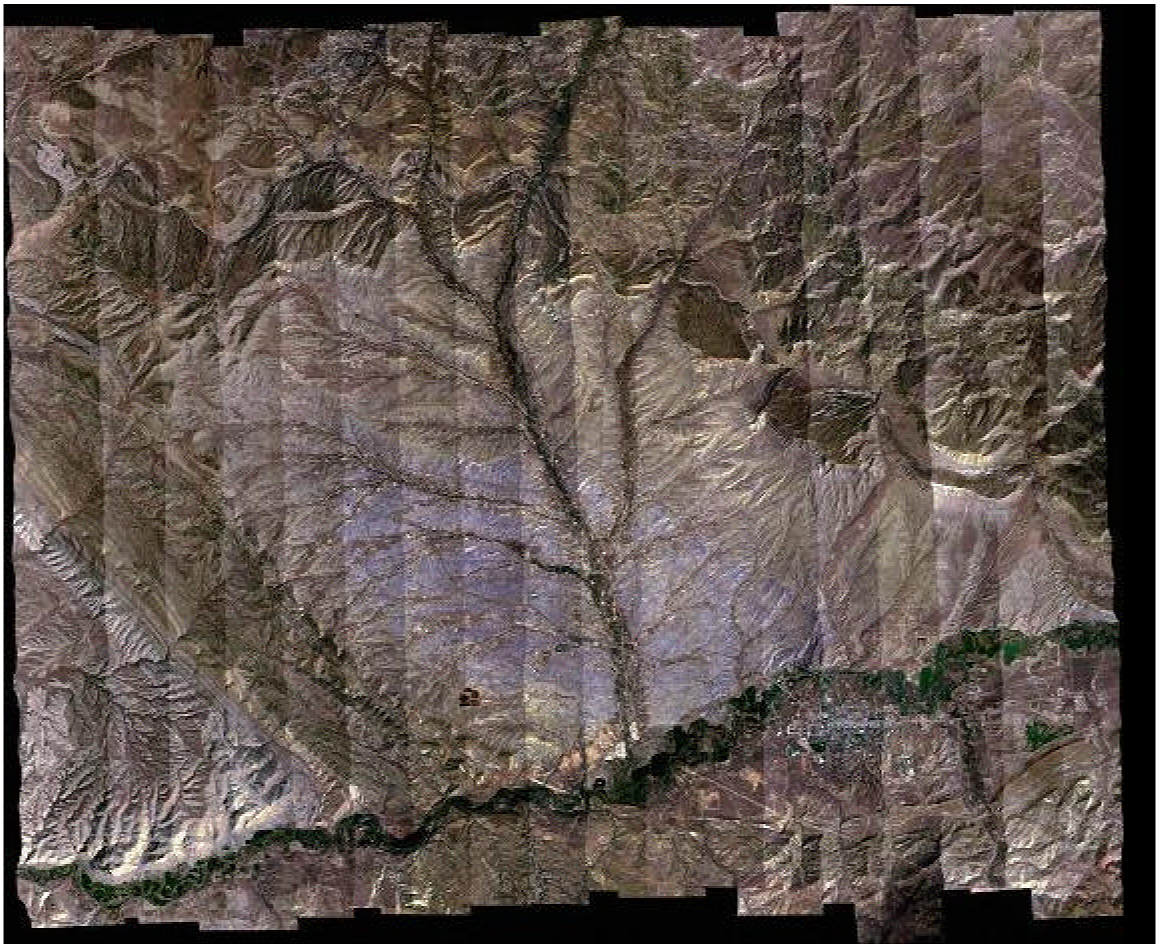

Figure 5 All the flight lines have been processed to produce and RGB almost true color image of the whole Rangely Oil Field basin, The surrounding formations and the town of Rangely. The individual flightlines are all georectified and there fore they can be mosiaced together to produce an image of the whole region.

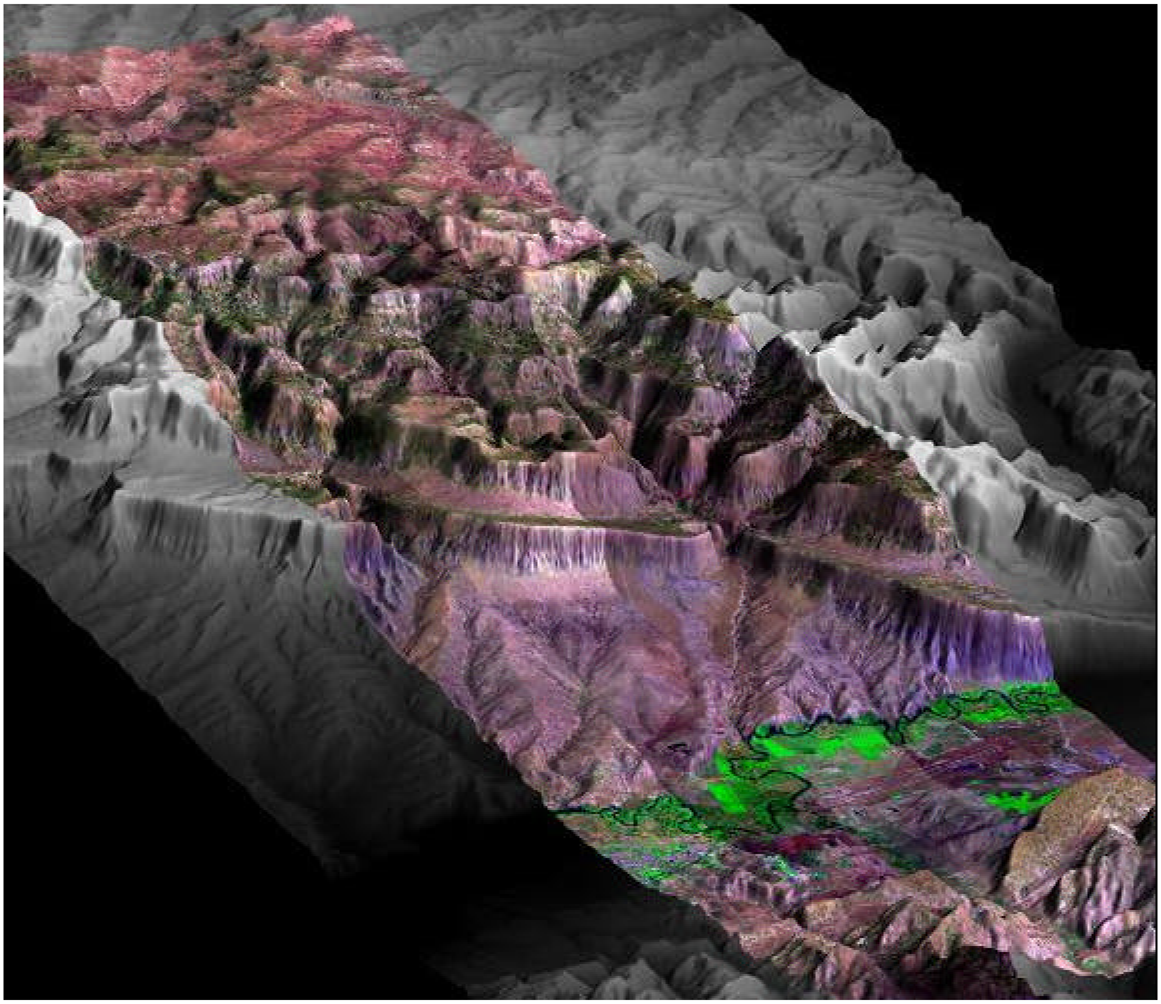

Figure 6 This is a Landsat image that has been draped over the Digital elevation model to produce a 3D image of the whole region.

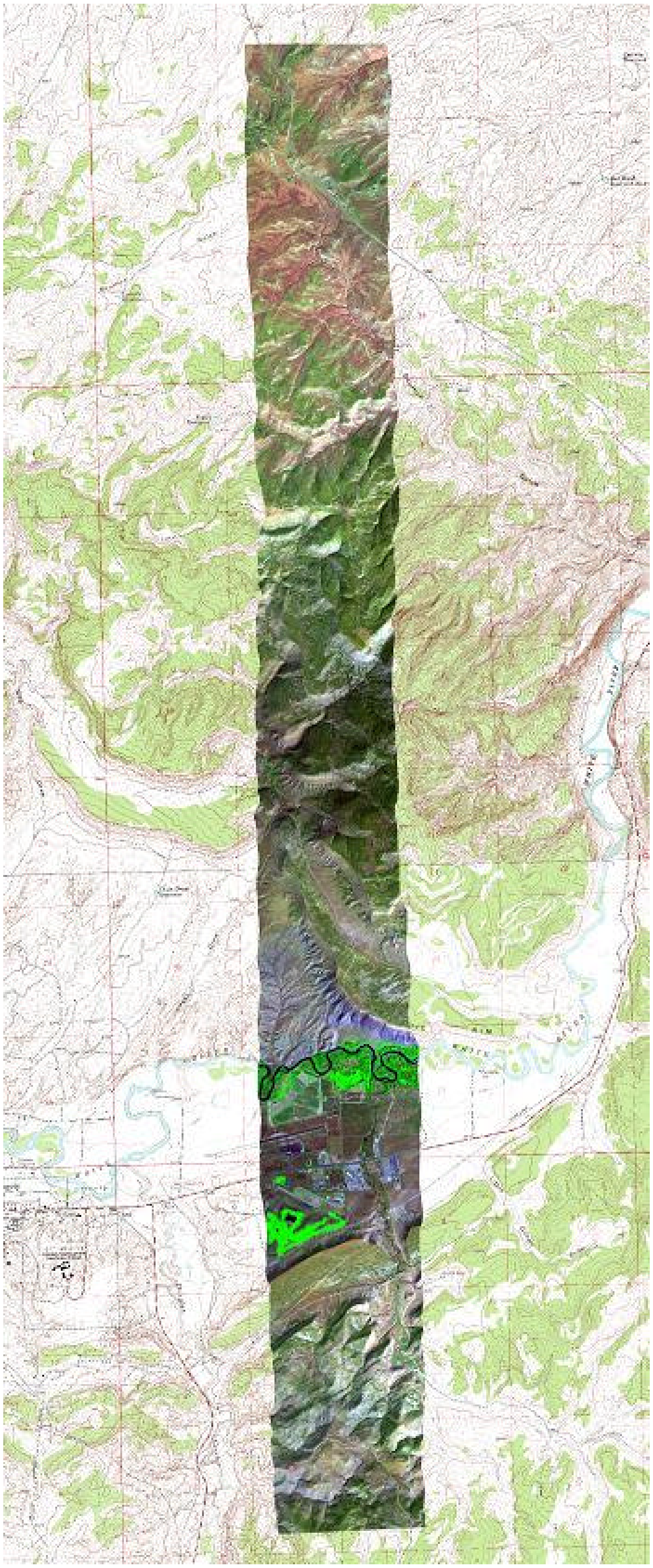

Figure 7 The USGS topographic map of Rangely with an overlaid RGB pseudo color image produced by analyzing flight line 16 (Peter Cocks, HyVista)

Figure 8 View of the Rangely oil field from on top of Mellen Hill. This is the area that was imaged in the top part of flightline 3. Our examples of detailed mapping in the oil field using the hyperspectral image analysis presented in the following Figures includes this area. Note well pads, roads, vegetation, and various soils.

Figure 9 Flight line 3 hyperspectral image analyzed using ENVI to produce a “true color” image shown on the left. The area includes the Rangely Oil Field shown in the photo previous figure. On the right there is a composite image of a map of what appears to be a mixture of Montmorillonite and Kaolinite mineral soils overlaid on a color infrared RGB produced from the hyperspectral image. Wendy Cover using the commercial image analysis program ENVI did this analysis. Wendy is a first year PH. D. graduate student at UC Santa Cruz in our remote sensing program. The procedure she used is complex and is referred to in the literature as the ENVI “hourglass” in the literature. If anyone is interested in finding out more about the procedure contact Wendy Cover or Bill Pickles. In our previous experience, these maps are extremely accurate in arid regions, which this is. The Montmorillonite Kaolinite soil mixture is shown in orange. The red color at the bottom of the image is the lush vegetation along the White River banks. It is red because the underlying image is a pseudo “color infrared” made from the hyperspectral image using the bands 27, 16, and 7 as red, green, and blue respectively. The true color image on the left was similarly made using the bands 15, 9, and 2 as RGB.

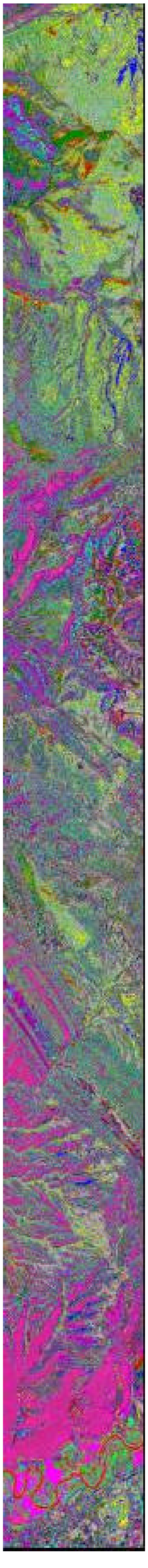

Figure 10 This is an "unsupervised classification" performed by Wendy Cover using ENVI in a different way. In this analysis, an algorithm separates the pixels in the image into some number of groups, in this case 35 groups. They are grouped so that the spectral signatures and brightness are most similar for the pixels in each group. I like to think of this process as what you would do if I asked you to sort a pile of multicolored "Indian corn" kernels into smaller piles where the kernels in the new piles were most like each other in size, colors, and patterns. As you went thru the process you would create more and more separate piles. Then if I asked you to limit the number of pile you would be forced to recombine piles. In recombining two piles you might decide to resort the piles along with several other piles to reduce the overall number of piles. This could iterate for a long time so at some point we would call halt to the process unless you had decided that the piles were not changing much between iterations. This is exactly what the unsupervised classification algorithm does using the brightness and spectral shapes in each pixel. This process is "blind" in that there is absolutely no information about what is causing the brightness or spectral shape in the pixels involved. This is always a wise step to take at the beginning of analyzing imagery of a new area, because it alerts you to the complexities of the region. This result is georectified as are all the analysis products after they are created. Therefore it can be used as very effective tool to sort out different types of soils, plants, etc, during a subsequent field trip to the site.

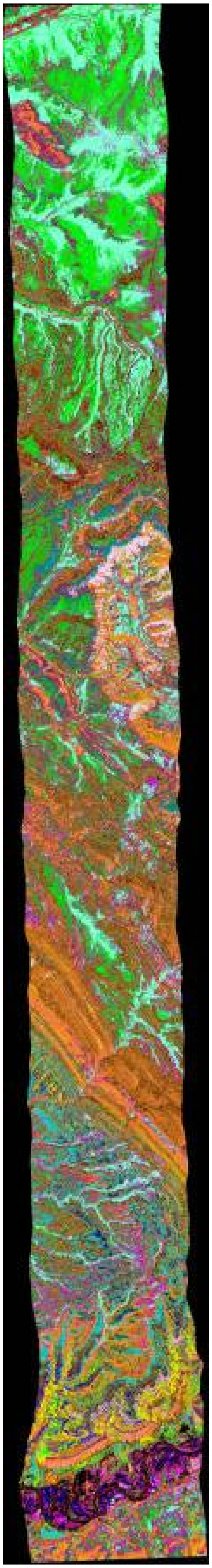

Figure 11 Spectral Angle Mapping (SAM) is another type of ENVI analysis and the result of applying this procedure to flightline 3 is shown at the left. Each one of the colors is a category produced by the SAM analysis. SAM analysis compares the spectral shapes in each pixel to the spectral libraries stored in ENVI. In this case we used USGS standard spectral libraries. We could use our own user generated spectral libraries which can be created from the image itself and or from spectra measured in the field at Rangely on our trip this coming August. Note that this analysis image is presented in georectified format.

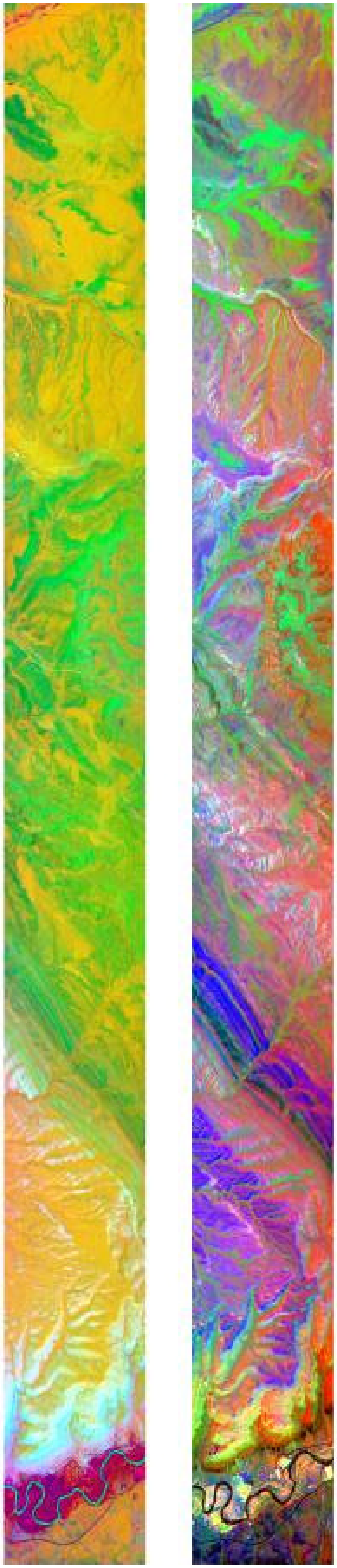

Figure 12 Analysis of the flight line 3 hyperspectral imagery using the ENVI Minimum Noise Fraction (MNF) procedure. In this procedure the original 128 bands of spectral information in each pixel are transformed into a new smaller set of objects that are referred to as MNF “pseudo bands”. They are not spectra any more, but they are “pseudo bands” that contain the most noise free information that was in the original hyperspectral image. MNF “ pseudo bands” 1,2,3 are presented as R,G,B in the image on the left. MNF pseudo bands 4,5,6 are presented on the right. Using these objects is where some real creativity on the part of the researcher is required. We will be using these analyses during our field trip to Rangely in August.

There are many analysis products such as these presented above, on the hyperspectral imagery of many of the Rangely flight lines. They are much to numerous to present here. The next step in our program is to return to Rangely with all the analyses in our laptops and start the verification process.

2.4.4.7 Conclusion

In Conclusion, we have had a very successful hyperspectral image acquisition at the Rangely Co Oil field. The imagery has been extensively analyzed. The results show incredible detail and complexity and detail in the mapping of soil types, plant species, plant health, water conditions, and human use features. This is very rich data set. Our new PH. D. Graduate student, who has been working on this analysis this year, is actually an environmental ecologist. We will be using the analysis to begin to develop a detailed understanding of the ecologies found at Rangely. This will provide a "snap shot" of the entire area as of August 2002. We are not certain if there is any evidence in the imagery analysis so far of plant life responses to CO2 leakage. However our field trip to Rangely this August will help use determine that more clearly. We do see evidence of what might be subtle hidden faults that could provide pathways for CO2 upward migration in the future. These need to be studied further and mapped over the whole field before commenting further on this matter.

2.4.4.8 References

We have many references that relate all our hyperspectral remote sensing programs with other hyperspectral programs worldwide. It is best to visit our website where many of these can be viewed and or downloaded for your use.

Our site is http://emerald.ucsc.edu/~hyperwww/instruments.html

There is also a remote sensing tutorial developed for and funded by Dr. Lucinda Jackson at ChevronTexaco, Richmond CA. Please visit this website, which is a version that is open to the public. http://es.ucsc.edu/~hyperwww/chevron/

2.4.4.9 Publications

We have many publications and presentations about all our hyperspectral remote sensing programs. It is best to visit our website where many of these can be viewed an or downloaded for your use.
Our site is http://emerald.ucsc.edu/~hyperwww/pubs.html

2.4.4.10 Bibliography

1. “Hyperspectral Remote Sensing for Research and Monitoring in Active Volcanic Regions”, B. A. Martini, E. A. Silver, W. L. Pickles, American Geophysical Union (AGU), San Francisco, paper V22F-05, December, 2000

2. “Use of hyperspectral sensing to obtain micro-scale ecological data on meso- to macro-scales”, Potts, D.C., Siciliano, D., Martini, B.A., Pickles, W.L. Silver, E.A., 9th Intl. Coral Reef Symp., 2000

3. “Hyperspectral applications across land-sea gradients from open ocean to watershed uplands”, Siciliano,D., Potts, D.C., Martini, B.A., Pickles, W.L., Silver, E.A., IEEE 2000 Intl. Geosci. Remote Sens. Symp., 2000

4. “High resolution hyperspectral sensing as an environmental monitoring tool for coastal and shallow marine habitats”, Siciliano, D., Potts, D., Marini, B., Silver, E., Pickles, W., 6th Intl. Conf. Remote Sens. Mar. Coast. Envir. [Best Paper Award], 2000

5. “Geological and Geobotanical Characterization of a Hydrothermal System Using Hyperspectral Imagery Analysis”, ERIM, Summer Meeting, Vancouver BC, B. A. Martini, S. A. Cochran, E. A. Silver, W. L. Pickles, D.C. Potts, July 1999

6. “New hyperspectral remote sensing techniques using geobotany, geology, and gas emission observations, for applied geothermal exploration and exploitation”, Martini, B.A., Cochran, S.A., Potts, D.C., Silver, E.A., Pickles, W.L., Carter, M.R., Priest, R.E., Wayne, B.M., White, W.T., Anderson, T., 13th Intl. Conf. Appl. Geol. Remote Sens., 1999

7. “Geological and Geobotanical Studies of Long Valley Caldera and Mammoth Mountain CA Utilizing New High Resolution Hyperspectral Imagery”, EOS, Fall AGU Meeting, San Francisco, CA, B.A Martini, Eli. A. Silver, W. L. Pickles, D. C. Potts, 1999

8. “Mapping environmental stress in Elkhorn Slough, central California using hyperspectral data: a management tool for an at-risk coastal ecosystem”, Cochran, S.A., Martini, B.A., Jacobs, J.R., Potts, D.C., Silver, E.A., Pickles, W.L., 5th Intl. Conf. Remote Sens. Mar. Coast. Envir., 1998

9. “Geological and Geobotanical Characterization of Hydrothermal System Utilizing Hyperspectral Imagery Analysis”, EOS, Fall AGU Meeting, San Francisco, CA, B.A Martini, S. A. Cochran, Eli. A. Silver, W. L. Pickles, D. C. Potts, 1998

10. “Detecting Plant Metabolic Responses Induced by Ground Shock Using Hyperspectral Remote Sensing and Physiological Contact Measurements”, W. L. Pickles, G. A. Carter, UCRL-ID-127061, December 3, 1996

11. “Observations of Temporary Plant Stress Induced by the Surface Shock of a 1-Kt Underground Explosion”, William L. Pickles, UCRL-ID-122557, December 4, 1995, available through National Technical Information Service, U.S. Dept of Commerce, Springfield, VA 22161

12. “Low Altitude Overhead Imagery Acquisition Pre-and Post-NPE”, William L. Pickles, LLNL, Janet E. Shines, David L. Hawley, Michael D. Pelan, and Stanley B. Brewster, Jr., EGG RSL, Proceedings of the Symposium on the Non-Proliferation Experiment: Results and Implications for Test Ban Treaties, pages 8-63 through 8-70, CONF 9404100, April 19-21, 1994

2.4.4.11 List of Acronyms and Abbreviations

Not Available at this time

2.4.5 Noble Gas Isotopes for Tracing CO2 Migration

Report Title

CO_2 Capture Project - An Integrated, Collaborative Technology Development Project for Next Generation CO_2 Separation, Capture and Geologic Sequestration

Noble Gas Isotopes for Tracing CO2 Migration

Report Reference

2.4.5

Type of Report:	Semi-Annual Report
Reporting Period Start Date:	February 2003
Reporting Period End Date:	July 2003
Principal Author(s):	Gregory Nimz
Date Report was issued:	August 2003
DOE Award Number:	DE-FC26-01NT41145
Submitting Organization:	Lawrence Livermore National Laboratory
Address:	7000 East Avenue Livermore, California 94550

2.4.5.1 Abstract

Noble gases can be dissolved into CO_2 being injected into geological formations for long-term storage and be used as tracers when monitoring for CO_2 leakage or subsurface migration. Stored CO_2 will be a supercritical liquid and the noble gases will remain dissolved in that liquid. Using them as tracers in this form is similar to using any common type of chemical tracer. However, leaking CO_2 migrating to the Earth's surface will become a gas and it is here that the noble gases become unique and highly valuable tracers. When the CO_2 becomes a gas, the noble gases will also be in the gas state and will migrate along with the CO_2 to the Earth's surface. They thereby become tracers of CO_2 gas migration. Because detection of certain noble gas isotopes is much more sensitive than CO_2 detection itself, the noble gases become an early warning of CO_2 leakage – long before there is enough surface CO_2 to cause vegetation distress, and long before elevated CO_2 levels would be noticed by surface CO_2 monitoring. There is even evidence to suggest that released noble gases would reach ground surface before released CO_2, enhancing the early warning capability. The objective of this project is to develop the technological foundation for utilizing noble gas isotopes to: 1) create a mechanism for long-term monitoring of CO_2 storage sites; 2) screen depleted oil fields, brine aquifers or similar formations for suitability for CO_2 storage (i.e., for their potential for leakage); and 3) provide a mechanism for fingerprinting injected CO_2 so that the source and ownership of leaking or subsurface migrating CO_2 can be identified. We have already successfully employed noble gas isotopic tracing in shallow groundwater systems (<1000' depth), and the developmental process of this project is an attempt to extend these techniques to CO_2 injection. The challenge involves characterization of noble gas behavior in a multiphase system (supercritical CO_2, $CO_{2\,(gas)}$, multiple hydrocarbon phases, and formation brines) under lithostatic pressures found at depths exceeding 5000 feet.

2.4.5.2 Table of Contents

2.4.5.3 List of Graphical Materials

2.4.5.4 Introduction

The noble gases (helium, neon, argon, krypton, xenon) all have multiple isotopes (atoms of the same element with different numbers of neutrons) that occur naturally on Earth. While the atomic ratios of the various noble gas isotopes to one another are generally very similar throughout the planet and atmosphere, there are regions or "compartments" that have unusual isotopic ratios. These unusual ratios "fingerprint" the noble gases as having originated in those compartments. Importantly, the CO_2 currently used for Enhanced Oil Recovery (EOR) injection (e.g., from Sheep Mountain or McElmo Dome) has natural characteristic noble gas isotopic fingerprints that are distinct from those found elsewhere in the Earth's crust. Should an anomalous isotopic signature be detected adjacent to an EOR reservoir, it would be a clear indication that injected gases are leaking. Noble gases therefore present a mechanism for monitoring presently used EOR reservoirs where caprock integrity is questionable due to production-related changes in their geologic formations.

A similar circumstance can be artificially created for injected (stored) industrial CO_2 by adding (spiking) noble gas isotopes of distinctive isotopic composition to the CO_2 prior to injection. We have been using artificial noble gas isotope tracers for the past 7-8 years in 3 separate, multi-kilometer scale groundwater recharge investigations tracking water volumes on the order of 10^8 m^3. LLNL is the only facility in the world currently doing noble gas isotope tracing. Only small amounts of spike are needed. For example, we can detect ^{124}Xe spike at concentrations as low as 1 part in 10^{15} by volume in CO_2. For injection quantities at the Rangely site (~1200 Bcf), only 35 cm^3-STP (standard temperature and pressure: 25ºC, 1 atm) of ^{124}Xe spike would be required at a cost of about $10000. For this reason, the tracers are practical to use; in our previous use of tracers in groundwater, the cost per tracer has been about $1 per million liters of water. As a means of confirmation during monitoring, or examining multiple pathways, multiple isotopes can be used. We have used ^{22}Ne, ^{78}Kr, ^{86}Kr, ^{124}Xe, ^{129}Xe and ^{136}Xe routinely. We have also used ^{126}Xe and ^{131}Xe (about 3 times the cost).

Since they are not radioactive and are chemically inert, noble gas tracers are persistent and stable in any environment. After injection (storage) of CO_2 spiked with noble gas isotopes, the region surrounding and above the storage site could be monitored to detect the distinctive noble gas isotopic signatures for decades to millennia. Because CO_2 will always be detected within the Earth's crust, the question for monitoring purposes will be whether its origin is natural or from injection. The isotopic signature of the noble gases measured with the CO_2 will indicate whether or not the gases originated within the storage site.

The project is divided into three components. The first utilizes the unique isotopic compositions of the noble gases dissolved in CO_2 currently being injected for EOR purposes in the Permian Basin as an initial test of the feasibility of CO_2-noble gas tracing. The second component designs a proof-of-principle field test in which noble gas tracers are added to injected CO_2 and the site is monitored for tracer breakthrough and/or CO_2 leakage. The third component addresses the question of how monitoring for leaking noble gases at the Earth surface would most effectively be accomplished; a series of numerical model simulations are being created for this purpose. These components are discussed in the following.

2.4.5.5 Executive Summary

2.4.5.5.1 Project Component I: Noble gas analysis of CO_2 floods from an Enhanced Oil Recovery field

The CO_2 currently being used for EOR flooding in the Permian Basin is primarily derived from a small number of naturally-occurring CO_2 deposits in northern New Mexico and southern Colorado (e.g., Bravo Dome, McElmo Dome, and Sheep Mountain). The isotopic compositions of the noble gases dissolved in the CO_2 from these sites is very unique, and unlike common noble gas compositions encountered in the Earth's crust and atmosphere. This is evident in neon and xenon isotopes (Figure 1; data from Caffee et al., 1999, and Phinney et al., 1978).

Figure 1. Neon and Xenon isotopic compositions from CO_2 used in the Permian Basin.

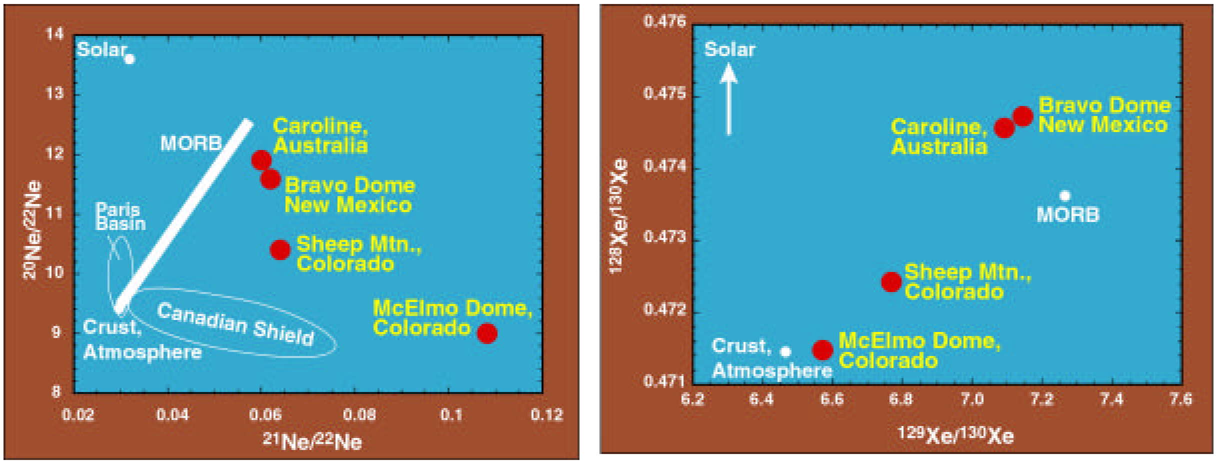

Because the compositions are unique, we can use active EOR fields as analogues to CO_2 storage sites. The noble gas "tracer" has already been added to the CO_2 being injected to enhance oil recovery. The CO_2 coming back to ground surface in the oil production wells can be tested and analyzed as though it were escaped CO_2 that has migrated to the surface. This allows us to address several questions: What is the concentration of noble gases in the returned CO_2? What percentage of noble gases injected with the CO_2 makes it back to the surface? Are the distinctive isotopic compositions retained in the returned CO_2? Which noble gases show the strongest signal (i.e., make the best tracer)? The tests also help us determine the quantities of noble gas tracer required for storage. In contrast to the natural CO_2 used in the Permian Basin, industrial CO_2 will contain little or no dissolved noble gas. Thus determining the amounts of noble gas to be added as tracer is important.

As a test location we have chosen the Mabee EOR field in west Texas, a few miles north of Midland. The Mabee field is owned and operated entirely by ChevronTexaco, who have kindly provided access to the field and help with logistical matters (Figure 2).

Figure 2. Location of the Mabee EOR field, Permain Basin, west Texas. The vast pipeline delivering natural CO_2 from the New Mexico and Colorado CO_2 domes is shown.

Eleven production wells were sampled, along with CO_2 from the feeder pipeline and CO_2 from a return pipeline of captured CO_2 that is to be reinjected. The results, discussed in Section 2.4.5.7 below, show that noble gas isotopic tracers will work extremely well as monitors of CO_2 leakage and subsurface migration. The isotopic compositions are easily detected and the gases retain the signal of the injected CO_2. The Mabee EOR test was very successful in providing the answers to the questions we targeted in this component of the project.

2.4.5.5.2 Project Component II: Design of a proof-of-principle tracer injection demonstration

Most greenhouse gas CO_2 is derived from industrial sources that do not contain dissolved noble gases with unique isotopic compositions. For these, a noble gas isotopic tracer will have to be added to the CO_2 during injection. The tracer will give the CO_2 a unique noble gas isotopic composition. One of the goals of this project, and one of the primary reasons to measure the noble gases at the Mabee field, is to determine the quantities of noble gas tracers that will have to be injected, and to design an injection methodology. The Mabee results allow us to decide which noble gas tracers will be the most useful, and to calculate the quantities required for surface monitoring. With these calculations, we can design a proof-of-principle tracer injection demonstration that will allow us to demonstrate the usefulness of noble gas tracers for CO_2 storage. This tracer demonstration could occur at either a prospective CO_2 storage site, or at an EOR field such as Mabee.

We have completed the calculations for tracer amounts and monitoring expectation, and these will be discussed in Section 2.4.5.7 below. The planning for a field demonstration will also be discussed in a document to be submitted to the CO_2 Capture Project at the end of this project. However, due to the budget reduction for this project, as developed during the Santa Cruz program meeting and communicated to us during the beginning of this reporting period, we will not be able to attempt an actual field demonstration. This change in work scope was agreed to by the CCP in March of this reporting period.

2.4.5.5.3 Project Component III: Numerical model simulations of CO_2/noble gas migration to the Earth surface

CO_2 that begins to leak from an underground storage site may initially still be supercritical (liquid), but will eventually become gas as it rises to the Earth surface and lithostatic pressures drop. During this process, there is potential for separation of the noble gases from the CO_2. How the noble gases and CO_2 will behave during migration to the Earth surface is not scientifically well known at present. The process is very complex, involving such questions as the mode of transport (e.g., by porous diffusion vs. fracture flow) and interaction with materials during transit (aquifer waters, hydrocarbons, rock). There are reasons to believe the noble gases may actually arrive at the surface before the escaped CO_2, in which case they would provide a precursory warning. One of the goals of this project is to investigate possible noble gas Earth surface monitoring strategies. Only by knowing how we will want to monitor can we make final decisions concerning which noble gas tracers to use, and how much tracer will have to be injected.

The behavior of the noble gases relative to CO_2 in the crust can be investigated using numerical simulation of fluid flow. A component of this project was to create a series of simulations that will help us design monitoring strategies at the Earth surface. As a starting point, a series of simulations could be used that were done at LLNL a few years ago for a study that examined noble gas flow from a release 600 feet below Earth surface. The simulations used the NUFT fluid transport code developed at LLNL. The code was able to accurately reproduce the arrival times of both SF_6 and ^3He (Figure 3; red circles represent gas detection, open circles represent no detection). We regard this study to be an analogue to CO_2 leakage from a subsurface storage site, and are using the NUFT code for our transport simulations. The SF_6-^3He study was published in the journal Nature (Carrigan et al., 1996).

Figure 3. Ground surface detection of ^{3}He and SF_6 from a release 600 feet deep, relative to release date.

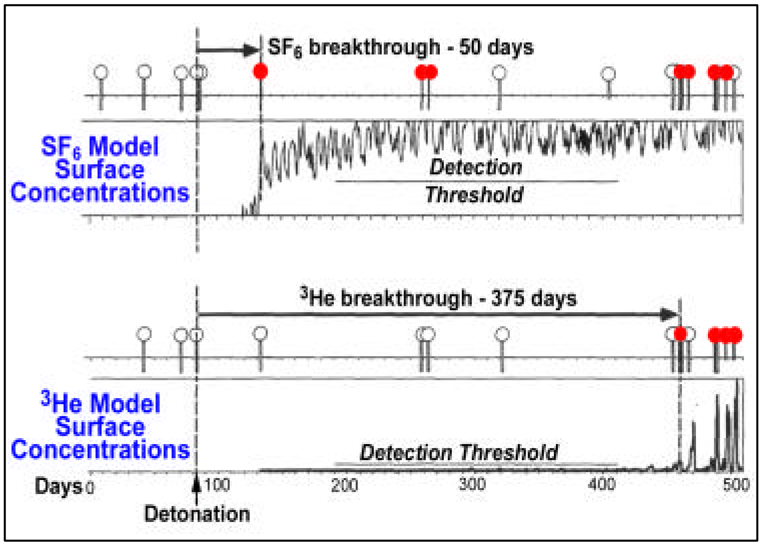

As a context for modeling, we have chosen the geological and hydrologic setting of the Permian Basin, as exemplified particularly by the Mabee EOR field. This was chosen obviously to dovetail with the results from Component I of this project. We have designed a two-dimensional model grid with nodes representing geological and hydrological features pervasive in the Permian Basin. Several model sensitivity actualizations have been completed. Our plan has been to enhance this model through addition of site-specific and high resolution subsurface data supplied to us ChevronTexaco, the operators of the field. For this, a nondisclosure agreement had to be executed, a process which has taken almost a year. An agreement signed by both LLNL and ChevronTexaco was completed on July 8th, 2003.

2.4.5.6 Experimental

The noble gas lab consists of two VG5400 noble gas mass spectrometers. The first spectrometer is set up to analyze xenon isotope ratios with very high precision. Major isotope ratios (^{129}Xe, ^{131}Xe, ^{132}Xe, ^{134}Xe and ^{136}Xe) are reproducible in air and water standards at 0.01%. This instrument is also used for precise $^{3}He/^{4}He$ measurements and the determination of tritium by the ^{3}He in-growth method. The second spectrometer is dedicated to measuring large variations in isotope ratios and samples with high ^{3}He, ^{4}He and high tritium. This instrument also performs isotope dilution measurements of He, Ne, Ar, Kr and Xe abundances and is a general-purpose system. Both spectrometer systems have automated, multi-port, sample processing systems able to handle gas and water samples. High temperature vacuum furnaces are available for the analysis of noble gases trapped in solids.

In addition to these traditional instruments, we have two membrane-inlet mass spectrometers (MIMS) dedicated to making continuous, real-time measurements of dissolved gases in water. The primary focus is to measure O_2, N_2 and Ar with high precision. We also measure dissolved H_2, CH_4, CO_2, He and Kr. One of the MIMS is portable and can be used in the field to assess sampling procedures and make determinations of the degree of gas saturation and measure radiogenic ^{4}He concentrations.

For health and safety reasons, as well as logistical simplicity, we have used a contractor laboratory in Midland, Texas to collect the CO_2 samples at the Mabee EOR field.

2.4.5.7 Results and Discussion

As anticipated, the isotopic compositions of the noble gases dissolved in the CO_2 sampled from the Mabee productions wells (derived mostly from McElmo Dome in this case), reflects the unique isotopic compositions of the injected pipeline CO_2. This is true of all the noble gases analyzed (we have made isotopic analyses for He, Ar, Ne, and Xe), and can be demonstrated here using argon (Figure 4).

Figure 4. Argon isotopic analyses of CO_2 from production wells at the Mabee EOR field. "KMCO2" is the analysis of pipeline CO_2 prior to injection; "Blend CO2" is CO_2 that was produced from all of the wells and combined for reinjection.

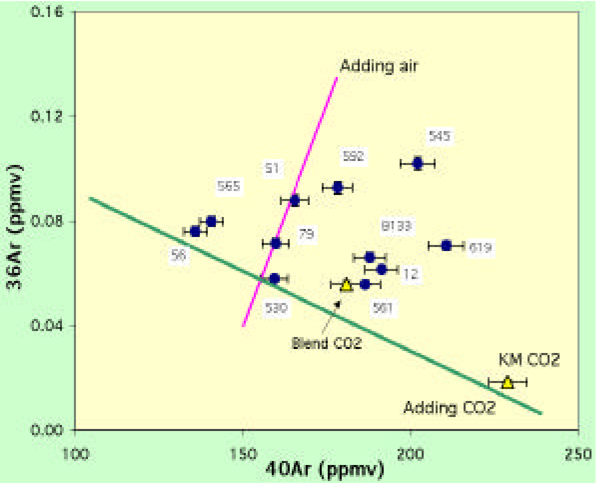

The argon isotopic systematics show that two other noble gas components are present. These are compartments of noble gases that occur in the subsurface in addition to the injected CO_2 compartment. The first is composed of the natural ambient noble gases - those within the formation prior to oil production (low ^{40}Ar and moderate ^{36}Ar - near the left end of the green line in the diagram). It is interesting that after years of oil production, including years of EOR flooding, this component can still be observed in the gases drawn from the production wells. The second compartment has the isotopic compositions characteristic of the Earth's atmosphere ("air" - high ^{40}Ar and ^{36}Ar, in the upward direction indicated by the magenta line in the diagram). We did not anticipate this component to be as evident as it is in the data set. This component is derived from the water that is injected in alternate sequences with the CO_2. The water helps to "guide" the CO_2 and further enhances oil recovery. This water is apparently derived from near-surface aquifers and contains dissolved atmospheric noble gases. The CO_2 from the combined, recycle pipeline (to be reinjected) has noble gas isotopic compositions that reflect an "average" of the three isotopic components ("Blend CO2" on the diagram).

The results of the Mabee isotopic analyses demonstrate that although subsurface changes can occur in the isotopic compositions, the signal from the injected CO_2 will be clearly in evidence. In a CO_2 storage setting, this signal in fact will be enhanced because the water component will not be present (water will not be injected along with the CO_2).

The Mabee results also allow us to design a proof-of-principle tracer test, to be conducted at a future date, through calculations of the test conditions. We believe helium and xenon isotopes would be best for the demonstration, because sensitivity is best for these and smaller amounts of tracer will be required. An example of these calculations is informative. Assuming: (1) the stored CO_2 is injected at 1140 MCFPD, equivalent to Mabee well 361AW; (2) the tracer is injected over a 24 hour period; and (3) the signal being monitored at the surface represent a soil CO_2-to-leaked CO_2 ratio of 100:1, then the amount of ^{3}He to be